Monocyte recruitment to endothelial cells in response to oscillatory shear stress

TZUNG K. HSIAI,[†,1] SUNG K. CHO,[§] PAK K. WONG,[§] MIKE ING,[†] ADLER SALAZAR,[†] ALEX SEVANIAN,[‡] MOHAMAD NAVAB,[*] LINDA L. DEMER,[*] AND CHIH-MING HO[§]

[†]Department of Biomedical Engineering and Division of Cardiovascular Medicine, USC School of Engineering and Keck School of Medicine, Los Angeles; [§]Department of Mechanical and Aerospace Engineering, UCLA School of Engineering and Applied Sciences, Los Angeles; *Division of Cardiology, Department of Medicine, UCLA School of Medicine, Los Angeles; and [‡]Department of Molecular Pharmacology & Toxicology, USC School of Pharmacy, Los Angeles, California, USA

ABSTRACT **Leukocyte recruitment to endothelial cells is a critical event in inflammatory responses. The spatial, temporal gradients of shear stress, topology, and outcome of cellular interactions that underlie these responses have so far been inferred from static imaging of tissue sections or studies of statically cultured cells. In this report, we developed micro-electromechanical systems (MEMS) sensors, comparable to a single endothelial cell (EC) in size, to link real-time shear stress with monocyte/EC binding kinetics in a complex flow environment, simulating the moving and unsteady separation point at the arterial bifurcation with high spatial and temporal resolution. In response to oscillatory shear stress (τ) at ± 2.6 dyn/cm^2 at a time-averaged shear stress (τ_{ave})=0 and 0.5 Hz, individual monocytes displayed unique to-and-fro trajectories undergoing rolling, binding, and dissociation with other monocyte, followed by solid adhesion on EC. Our study quantified individual monocyte/EC binding kinetics in terms of displacement and velocity profiles. Oscillatory flow induces up-regulation of adhesion molecules and cytokines to mediate monocyte/EC interactions over a dynamic range of shear stress ± 2.6 dyn/cm^2 (P=0.50, n=10).—Hsiai, T. K., Cho, S. K., Wong, P. K., Ing, M., Salazar, A., Sevanian, A., Navab, M., Demer, L. L., Ho, C.-M. Monocyte recruitment to endothelial cells in response to oscillatory shear stress. *FASEB J.* 17, 1648–1657 (2003)**

Key Words: micro-electromechanical systems (MEMS) · cell tracking velocimetry · shear stress sensors · endothelial cells · monocytes

The process of leukocyte adhesion to endothelial cells (EC) involves a complex balance of forces arising from hydrodynamic shear effects and the dynamics of leukocyte/ endothelial cell (EC) binding. The endothelium, which lines the inner lumen of blood vessel walls, is intimately involved in the recruitment of leukocytes fundamental to the initiation of immune responses (1, 2). Shear stress, the tangential drag force of blood passing along the surface of the endothelium (3), imparts profound effects on endothelial cell (EC) function (4–6). Around arterial bends and branches in which the inflammatory responses prevail, the fluid mechanical environment is distinct from the laminar pulsatile environment present in the long, straight sections of the vessel wall. Oscillatory flow with a time-averaged shear stress of 0, characteristic of reattachment points in the arterial branches, modulates the biological activities of EC (7–9). Leukocyte rolling, adhesion, and transmigration have been observed in response to inflammatory stimuli at the microvascular levels (10). What is warranted is a dynamic, high spatial and temporal resolution view of these events in a more complex physiologic flow environment. Therefore, we have developed specialized micro-electromechanical systems (MEMS) sensors and cell tracking velocimetry to link spatial and temporal resolution of real-time shear stress with the monocyte/EC binding kinetics, simulating reattachment points at arterial bifurcations (11).

No direct measurement has been achieved to resolve the spatial and temporal variations, albeit evidence exists for direct correlations of shear stress with distribution of focal atherosclerotic lesions (12) and the computational fluid dynamic (CFD) determinations of shear stress in the arterial circulation (13, 14). MEMS, which are derived from semiconductor technology, enable the realization of highly miniaturized mechanical devices such as sensors and actuators. We developed and fabricated MEMS shear stress sensors, nearly the size of an elongated EC, based on heat transfer principles. Heat transfer from a resistively heated element of the sensor to the flowing fluid was measured, allowing determinations of shear stress level from a linear relation between V^2 (V = voltage) and $\tau^{1/3}$ (15). By simulating oscillatory flow at the unsteady and moving separation point of arterial bifurcations (16), we were able to link real-time shear stress with the trajectory patterns of monocyte/EC binding kinetics. We found that individual cell–cell interactions occurred over a range of shear stress of ± 2.6 dyn/cm^2. While both

[1] Correspondence: University of Southern California, Olin Hall of Engineering 500, Los Angeles, CA 90089-1451, USA. E-mail: hsiai@usc.edu

doi: 10.1096/fj.02-1064com

0892-6638/03/0017-1648 © FASEB

biochemical and biomechanical forces are synergistic in the regulation of cell–cell binding kinetics, the relative levels of these two forces may be dependent on the geometric configuration of arterial circulation and the local flow milieu.

MATERIALS AND METHODS

MEMS shear stress sensors operating principles

The operation of this shear stress sensor is based on the fully developed flow condition in which the rate of heat loss from a heated resistive element to the fluid flow is dependent on the velocity boundary layer profile (17). The change in temperature of the local flow milieu leads to the change in resistivity of the sensors.

The dynamic performance of the sensors is characterized by a three-layer structure (**Fig. 1*a***): *1)* the sensing element or the film layer is the top layer; *2)* the silicon nitride diaphragm in the middle is an insulation layer, and *3)* the silicon substrate at the bottom serves as heat sink. From Fig. 1*a*, the energy balance equation is expressed as (18):

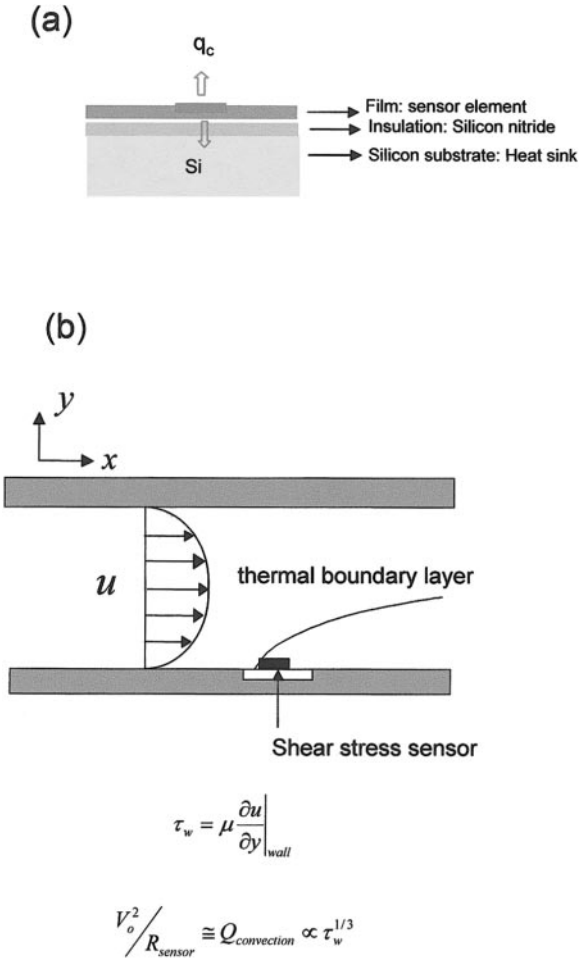

Figure 1. Principle of thermal shear stress sensors. *a)* Three-layer model. For heat transfer "q_c" refers to convective heat transfer. *b)* The thermal element resides within a velocity boundary layer. The rate of heat loss from a heated resistive element to the fluid flow is dependent on the velocity profile in the boundary layer. A linear relation is obtained as $V^2/R \propto \tau^{1/3}$ based on heat transfer principles.

$$P = I^2R = c_f m_f \frac{dT_f}{dt} + c_i m_i \frac{dT_i}{dt} + h(u_\tau)A(T - T_0), \qquad (1)$$

where h denotes the heat transfer coefficient. The subscripts *f, i,* and *c* represent the convective heat transfer from the film and insulation layer to the measured fluid, respectively. T is the temperature of the sensor element and T_0 the heat sink. The product of the square of current, I^2, and the resistor sensor R gives rise to the heating power as i^2R. At a low frequency of cardiac cycles, the two unsteady terms in Eq. 1 are negligible. Thus, Eq. 1 can be simplified to set power dissipation to equal to the convective heat transfer term (from the heated sensor to the ambient fluid). The convective heat transfer coefficient is expressed as h (u_τ), where the shear velocity u_τ is related to wall shear stress as $\tau_w = u_\tau^2 \rho$, and ρ is the fluid density. The heating power for the sensor is related to the wall shear stress as (17):

$$P = h(u_\tau)A(T - T_o) = (a + b\tau^{1/3})(T - T_o), \qquad (2)$$

where a and b are calibration constants. The resistance, R, of a semiconductor sensing element is a function of change in temperature:

$$R = R_o(1 + \alpha(T - T_o)) \qquad (3)$$

where R_o is the resistance at room temperature T_o and α is the temperature coefficient of resistance (TCR). An important feature governing the thermal shear stress sensor operation is the temperature over-heat ratio, α_T, defined as the relative change of sensor temperature compared with the ambient temperature:

$$\alpha_T = (T - T_o)/T_o \qquad (4)$$

It is also commonly defined as resistance over-heat ratio as, α_R, which reflects the relative change of sensor resistance compared with the resistance at the ambient temperature,

$$\alpha_R = (R - R_o)/R_o \qquad (5)$$

The resistance over-heat ratio was set at 0.12 in order to minimize natural convection by the heating of the resistive element.

Given $p = V^2/R$, where V is the voltage across the sensor, Eq. 4 becomes

$$V^2/R = (a + b_T\tau^{1/3}). \qquad (6)$$

The temperature coefficient of resistance (TCR or α, Eq. 3) is dependent on the concentration of boron doped into the polysilicon strip. The measured TCR (temperature coefficient of resistivity) of the sensor was ~0.1%/°C for high doping level at $10^{16}/cm^2$ and 60 keV of energy (18). In a fully developed channel flow, the flow shear stress determines the rate of heat transfer from a heated resistive element to the surrounding fluid field. The heating power is proportional to convective heat transfers. Thus, a linear relation between V^2 and $\tau_w^{1/3}$ is established (Fig. 1*b*).

MEMS shear stress sensor design

The schematic diagram of the sensor (**Fig. 2**) features the polysilicon as the heating and sensing element at the center of a cavity diaphragm. The polysilicon, measuring 2 μm wide, 0.5 μm high, and 80 μm long, was uniformly doped with boron to a low sheet resistance value of 50 Ω/cm^2 to a typical resistance of 1.25 ~ 5 kΩ at room temperature. After doping, the wafer was annealed at 1000°C to activate the dopant and to reduce the intrinsic stress on the polysilicon. The resis-

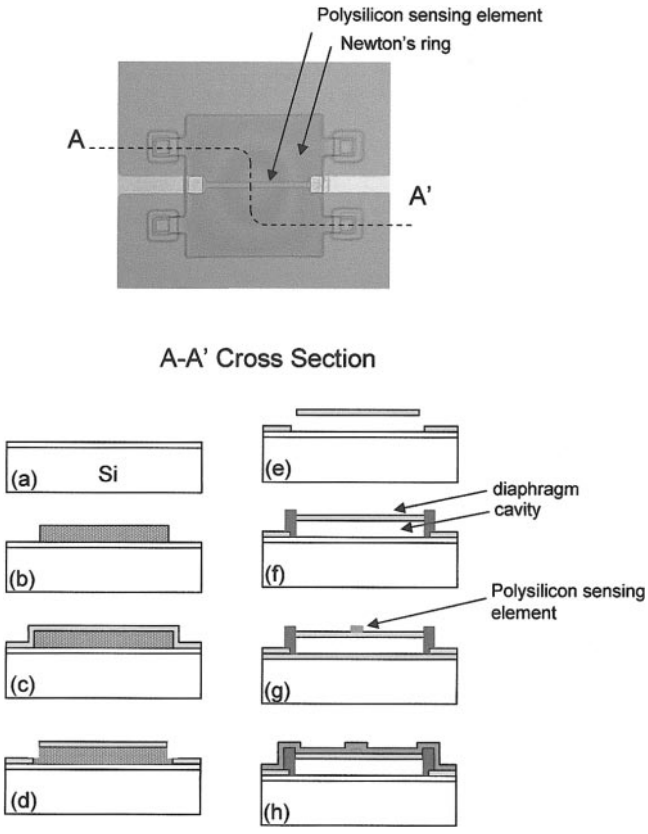

Figure 2. Fabrication steps of the microthermal shear stress sensor. *a)* Thermal oxidation and Si_3N_4 deposition; *b)* polysilicon deposition and patterning; *c)* thermal oxidation and Si_3N_4 deposition; *d)* opening etching holes; *e)* removing the sacrificial poly-Si layer; *f)* blocking the etching holes; *g)* poly-Si deposition, ion implantation with boron and patterning; *h)* Al deposition and patterning for electrodes and SiO_2 deposition for waterproof.

tance of the sensing element could be adjusted by changing the doping levels. The optimal resistance for the MEMS shear stress sensor ranged from 1 to 10 kΩ, higher than that of the traditional metal sensor (5 to 50 Ω). This unique resistance level gave rise to a high-frequency response.

An array of resistors was fabricated on a single chip while each individual resistor was lying across the diaphragm (Fig. 2*f*). The diaphragm was separated from the bottom of the cavity by an ~2 μm gap while the pressure inside the cavity was estimated at 300 torr. Thermal evaporation of the aluminum metallization (300 nm in height and 10 μm in width) forms the leads connecting the polysilicon resistor or the sensing element to the external electronics. The novel feature of the vacuum cavity was to generate effective thermal isolation between the heated element and the substrate, thereby minimizing the heat conduction from the diaphragm to the substrate through the gap (18).

MEMS sensor fabrication

The process flow involved both surface and bulk micromachining. Silicon nitride 100 nm in thickness was first deposited by low-pressure chemical vapor deposition (LPCVD) on a 4 inch wafer (Fig. 2*a*). LPCVD of a 1.4 μm sacrificial polysilicon layer was deposited and patterned (Fig. 2*b*), followed by thermal oxidation of the sacrificial layer at 800 nm (the first layer of diaphragm) (Fig. 2*c*). Deposition of 350 nm silicon nitride as the second diaphragm material was established by LPCVD (Fig. 2*d*). Next, etching holes were opened by removing two layers: silicon nitride by reactive ion etching (RIE) and the thermal oxide by buffered oxide etchant (BOE) (Fig. 2*e*). The sacrificial polysilicon was then removed by tetramethyl ammonium hydroxide (TMAH) at 80°C for 3 h. An oxide layer (1.2 μm) and silicon-nitride layer (300 nm) were deposited at 300 mTorr (0.04 Pa) to seal the cavity under vacuum, followed by patterning using both RIE and BOE (Fig. 2*f*).

Doping the polysilicon was done by ion implantation with boron at a total dose of $1 \times 10^{16}/cm^2$ (Fig. 2*g*). The wafer was then annealed at 1050°C for 1 h to activate the boron ions and to reduce the intrinsic stress of the polysilicon. With sputtering, aluminum metallization formed the leads (Fig. 2*h*). A 1.5 μm layer of LPCVD oxide was deposited for passivation of the polysilicon sensing element to prevent resistance drift from spontaneous oxidation. Since the cavity was held under vacuum, the diaphragm was bent down by the external atmospheric pressure, giving rise to an optical interference patterns referred as Newton rings in Fig. 2.

MEMS sensor calibration

Calibration was performed to establish a linear relation between V^2 and $\tau_w^{1/3}$. In the case of an unsteady state, we generated four individual pulsatile flows with different mean flow rates, Q_n. The averaged voltage output signals (V_n) from the MEMS sensor corresponded to the individual mean flow rates at 37± 0.15°C (data not shown). The shear stress values corresponding to these four individual flow rates were calculated using Eq. 7, and a linear relation between V^2 and $\tau^{1/3}$ was established (data not shown).

$$\tau_w = \left(\frac{6\mu}{h^2 w}\right) Q, \tag{7}$$

where w is the width of channel and μ is the dynamic viscosity of fluid.

Integrating MEMS sensors with a pulsatile flow channel

A novel pulsatile flow system delivered well-defined flow profiles simulating the flow conditions in the arterial circulation (19) (**Fig. 3**). This unique configuration ensured velocity uniformity and absence of flow separation across the width of the channel during flow reversal. Due to the symmetry of the rectangular flow channel, we were able to flush-mount the sensor opposite to the EC monolayers, which were seeded on the bottom parallel plate. This approach circumvents the local flow disturbance introduced by conventional probes.

Validation of real-time shear stress

Theoretical shear stress was obtained by using the Bernoulli's theorem with an orifice located upstream from the flow channel. The pressure signals were measured with a piezoelectric sensor at 10 Hz (SenSym Model 143SC03D). The signals were phase-averaged, then converted to the pulsatile flows. The experimental measurements by the MEMS sensors were validated against the theoretical formulation, which can be accessed at http://atvb.ahajournals.org (20).

Monocyte tracking velocimetry

We developed a cell tracking velocimetry algorithm (21) to reconstruct the trajectories of monocyte/EC interactions in response to oscillatory shear stress. The time-dependent

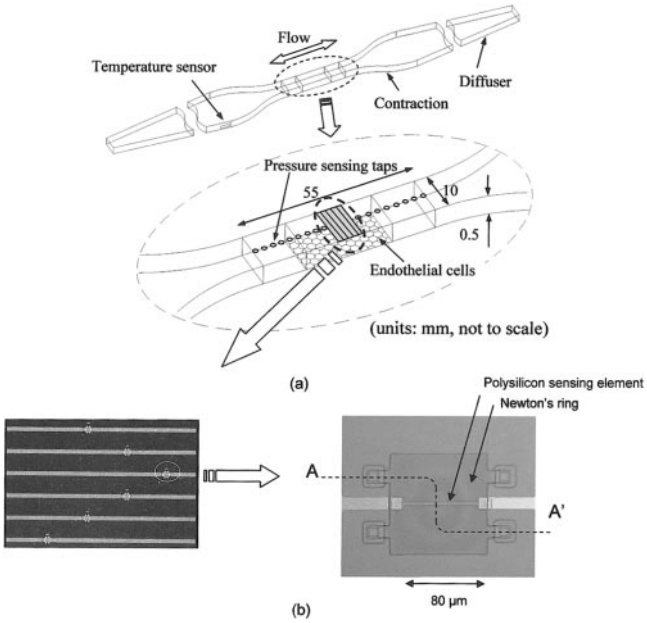

Figure 3. *a)* Test channel with the flush-mounted microthermal shear stress sensor array to the upper wall of the pulsatile flow channel. Confluent BAEC monolayers were seeded on the bottom. *b)* A photograph of individual shear stress sensors illustrate the polysilicon as an sensing element. The diaphragm (see Fig. 2*f*) was bent down by the external atmospheric pressure, giving rise to an optical interference patterns referred as Newton rings.

positions of monocyte/monocyte and monocyte/EC binding kinetics were recorded to videotape by a CCD camera and digitalized with a video capture card (Truevision TARGA 1000). The digital images were then analyzed by the velocimetry algorithms to capture precise monocyte locomotion in relation to the EC monolayers. The algorithm initiates the identification of monocytes by dividing the fields of interest into interrogation areas that are comparable to the size of individual monocytes. The fields of interest were sampled such that 50% the interrogation areas were overlapped to satisfy the Nyquist sampling criteria (22). Both the presence of monocytes and the center position of the cells in the interrogation area were determined by the convolution of the interrogation area with a typical monocyte image (**Fig. 4*a***). The displacement of the monocytes was extracted by 2-dimensional cross-correlation of the image area with the corresponding area in the next digital image. The peaks of the 2-dimensional cross-correlation signal provide displacement information of monocytes between different digital images (Fig. 4*b*).

Endothelial cell culture

Bovine aortic endothelial cells (BAEC) between passages 5 and 9 were seeded on Cell-Tak cell adhesive (Becton Dickson Labware, Bedford, MA, USA) and Vitrogen (Cohesion, Palo Alto, CA, USA; RC 0701) -coated glass slides (1 cm×5 cm) at 3×10^6 cells per slide. BAEC were then grown to confluent monolayers in DMEM (Dulbecco's modified Eagle's medium) supplemented with 20% fetal bovine serum, and 0.05% amphotericin B, and 100 U/mL streptomycin for 48 h in 5% CO_2 at 37°C.

Experimental protocols

Glass slides containing confluent BAEC were placed in the flow channel and exposed to one of the two flow conditions at 1 Hz for 4 h: *1)* pulsatile flow at a shear stress slew rate ($\partial\tau/\partial t$) of 293 dyne/(cm^2 s), with a time-averaged shear stress (τ_{ave}) of 50 dynes/cm^2 (**Fig. 5*a***), *2)* oscillating flow (±2.6 dynes/cm^2 at 0.5 Hz) with τ_{ave} = 0 dynes/cm^2 at 0.5 Hz (Fig. 5*b*). For oscillating flow, minimal forward flow at a mean shear stress of 0.2 dynes/cm^2 was provided every hour to deliver nutrients and remove waste products from the cells.

Real-time monocyte/endothelial cell interactions in response to oscillatory flow

Monocytes were isolated using a modification of the Recalde method as described previously (23) from normal volunteers with institutional review board approval. Freshly isolated monocytes (10^5 monocytes/cm^3) were introduced into the testing channel under oscillatory flow with parameters as described in Experimental Protocols. The flow channel was mounted on an inverted light microscope for a real-time monitoring of cell–cell interactions. Five percent CO_2 was delivered to the circulating culture medium. Monocytes and

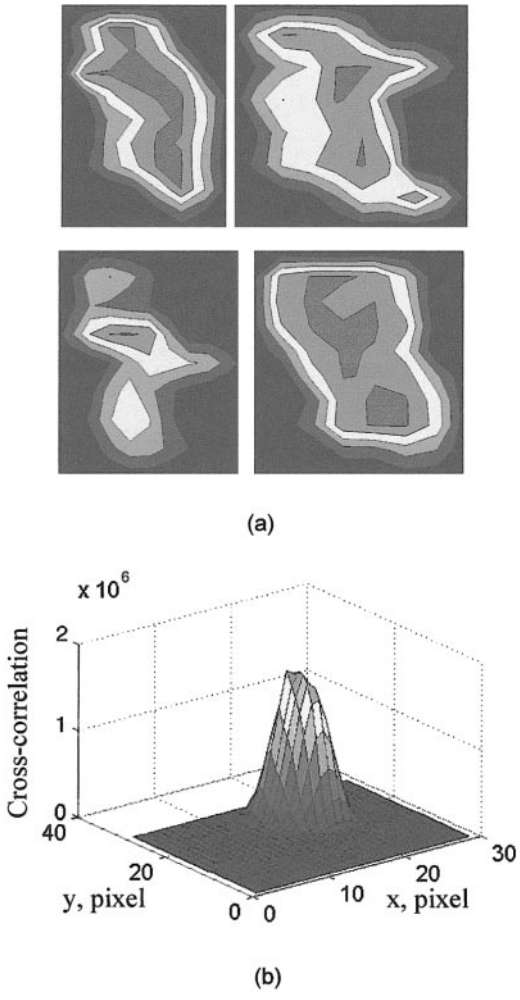

Figure 4. Cell tracking velocimetry: *a)* Intensity contours of monocytes obtained from digitized video images; *b)* representative cross-correlation for determining the monocyte displacement.

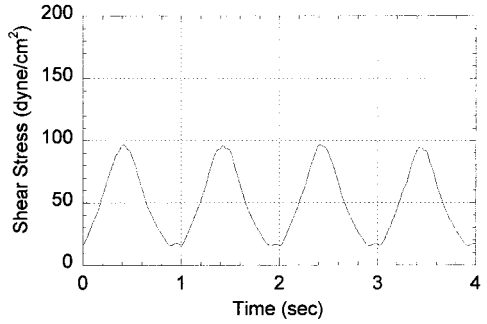

(a)

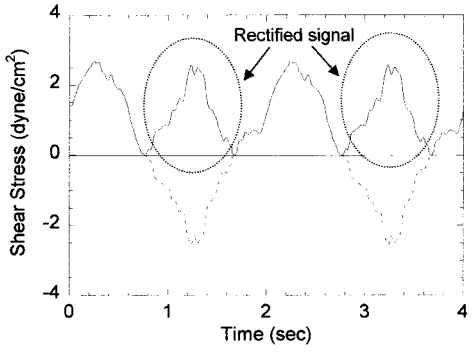

(b)

Figure 5. Real-time shear stress measurement by the microthermal shear stress sensors. *a)* Pulsatile flow; *b)* oscillatory flow to simulate the outer wall of arterial bifurcations at the reattachment point.

BAEC interactions in response to flow conditions were captured by phase contrast microscope (Nikon Eclipse TE 200), and transmitted by a CCD camera (SONY CCD-IRIS/RGB, Model DXC 151A) to a TV monitor. Imaging data collection spanned 12 h to visualize different stages of cell–cell interactions and tight association of cell–cell interaction throughout the observation period. Real-time shear stress at which different stages of cell–cell interactions occurred was linked with monocyte-monocyte binding and separation, monocyte tethering, and adhesion with the EC monolayers. At a given shear stress, the velocity of the flow field, which was calculated from Eq. 7, was compared with the individual monocyte velocities.

Monocyte adhesion assay

After 4 h of flow pulsatile vs. oscillatory flow conditions as described in Experimental Protocols, BAEC monolayers on the cover slides were rinsed with DMEM and assayed for monocyte binding activities. Endothelial monolayers were incubated with freshly isolated monocytes (10^5 monocytes/cm^2) for 10 min at 37°C under static conditions. Nonadherent monocytes were washed with DMEM. The adherent monocytes were fixed with 1% glutaraldehyde. Adherent monocytes were counted in a total of 20 high-power (400×) standardized fields.

Quantitative real-time RT-PCR

After BAEC were exposed to the flow conditions, total RNA was isolated using RNeasy kit (Qiagen, Chatsworth, CA, USA). Real-time RT-PCR was performed according to the recommendations of PE Biosystems TaqMan PCR Core Reagent Kit (24). Equal amounts of RNA at 0.5 μg/μL were reverse-transcribed to bring the mixed solution to a final concentration of 1× TaqMan buffer, 5 mmol/L MgCl2, 200 μmol/L dATP/dCTP/dGTP, 400 μmol/L dUTP, 100 nmol/L probe, 400 nmol/L primers, 0.01 U/μL AmpErase, and 0.025 U/μL AmpliTag Cold DNA polymerase. Total RNA at 0.4 ng/μL in 5 μL was then transferred to the 96-well plate. PCR was performed at 50°C for 2 min and at 95°C for 10 min, then run for 40 cycles at 95°C for 15 s and 60°C for 1 min on the real-time RT-PCR Engine (MJ Research Opticon®, Watertown, MA, U SA). Ct, which is the threshold cycle number at which the initial amplification becomes detectable by fluorescence. ΔR_n, normalizes fluorescence. TaqMan probes (25) were used for added specificity and sensitivity. Assuming amplification is 100% efficient, we used the difference in Ct values for various flow conditions vs. control to mathematically determine the relative difference in the level of P-selectin, intercellular adhesion molecule (ICAM-1), and MCP-1 mRNA expression (26). The primers (**Table 1**) were produced on an automated synthesizer (Applied Biosystems, Foster City, CA, USA) according to the manufacturer's protocol. For each gene, quantitative RT-PCR was conducted in duplicate. To ensure the quality of the measurements, negative and positive controls were systematically included in duplicate in each plate. The statistical analysis of the quantitative RT-PCR results was done using the ΔCt value ($Ct_{gene\ of\ interest}$-Ct_{GAPDH}). Relative gene expression was obtained by ΔΔCt methods (ΔCt_{sample}-ΔCt_{GAPDH}) using the control group as a calibrator for comparison of every unknown sample gene expression level. The conver-

TABLE 1. *Primers used for quantitative real-time RT-PCR*

Gene	Primer sequences and TaqMan® probes
P-selectin	Forward, 5′-GGGCCACTGACTATCCAGGA-3′
	Reverse, 5′-AACCCGTCACTAAGCCTGTTGT-3′
	5′-6(FAM)-ACCCTGACTTATGTTGGTGGAGCAGCA-3′
ICAM-1	Forward, 5′-CGAGAAGAGAGGACCATGGC-3′
	Reverse, 5′-GCCCTTGTGACCGCAGG-3′
	5′-6(FAM)-CCAATTTCTCTTGCCGCTGGGAACTG-3′
MCP-1	Forward, 5′-GAGGCCAAACCAGAGACCAA-3′
	Reverse, 5′-GCAGCGGAGACCTTCATGTT-3′
	5′-(FAM)-CACGCTGAAACTTGAATCCTCTCGCTG-(TAMRA)-3′
GAPDH	Forward, 5′-CCCACTCCCAACGTGTCTG′-3′
	Reverse, 5′-TCTTTGGACGGTTCATACTACTCTA′3′
	TaqMan probe 5′-TGTGGATCTGACCTGCCCGCCTG-3′

sion between ΔΔCt and relative gene expression levels is fold induction = $2^{-\Delta\Delta Ct}$ (26).

Statistics

The values of shear stress at which monocyte-monocyte binding and separation, monocyte-endothelial cell tethering, adhesion and detachment were expressed as mean values ± standard deviation. A nonparametric (Wilcoxon rank sum test) comparison of the groups (means of five cell–cell binding events) was applied. *P* value, which defined the 95% confident interval, was considered statistically significant at < 0.05.

RESULTS

Real-time shear stress by MEMS sensors

Two flow profiles representative of different sites at vascular branching points were generated: oscillatory flow and unidirectional pulsatile flow at high and low shear stress slew rates. Using the linear calibration curve (data not shown), we obtained real-time pulsatile vs. oscillatory shear stresses that were delivered to EC at 37.0 ± 0.15°C (Fig. 5*a*). The oscillatory pressure profile at an arbitrary periodicity of 0.5 Hz simulated the flow pattern seen at the reattachment points (Fig. 5*b*). This profile reflected the absolute pressure signals fluctuating between +2.6 and –2.6 dyn/cm^2 with $\tau_{ave} = 0$. The time-averaged shear stress (τ_{ave}) was 50 dyn/cm^2. The flow reversal was recorded as upward deflection by the sensor. We validated the real-time shear stress measurement using the Bernoulli's Principle with an orifice (19).

Nonlinear displacement of monocyte locomotion in response to oscillatory flow

The paths followed by monocyte locomotion were traced by cell tracking velocimetry, revealing diverse modes of cell–cell interactions in response to oscillating flow. Image sequences show the meandering paths of a monocyte at fluctuating velocity while undergoing to-and-fro rolling and firm attachment to the EC (**Fig. 6*a***). Under oscillatory shear stress, the irregularities of monocyte trajectory (Fig. 6*b*) may be due to the undulating surface topology of the EC monolayers and to the time variation in integrin–ligand bond formation and breakage. Two monocytes undergoing attachment, separation, short-lived reattachment, and reseparation with one another were captured (**Fig. 7*a–e***). Both monocytes briefly established anchorage on EC (Fig. 7*b*). Monocyte 2 then separated from monocyte 1, which eventually established anchorage on EC as illustrated at 0 reference point on the *y*-axis (Fig. 7*d*). The corresponding trajectories of these two individual monocytes were captured using cell tracking velocimetry (Fig. 7*f*). Monocyte 1 was observed to undergo tethering, characterized as abrupt halt in locomotion alternating with resumption of to-and-for motion. The trajectory of the nonviable monocytes that were buoyant above the EC monolayer contrasted with those of monocytes 1 and 2 (Fig. 7*f*). In the presence of oscillatory shear stress, the absolute displacement, velocities, and direction of monocytes were nonlinear, and nonrandom, implicating the dynamics of molecular interactions underlying the cell–cell binding kinetics. The rolling velocities of individual monocytes were distinct from the hydrodynamic velocity of the flow field near the wall of the channel and that of the nonviable monocyte (Fig. 7*g*). Unlike the velocity profile of nonviable monocyte, individual monocyte motion was retarded when they are in contact with the EC monolayers. Individual monocytes were observed to display binding and separation with other monocytes, transient tethers and solid attachment to the EC monolayers over a dynamic range of wall shear stress (±2.6 dyn/cm^2 at 0.5 Hz; **Fig. 8**). The mean shear stress values corresponding to the individual events were statically insignificant (n=10 events, P=0.50).

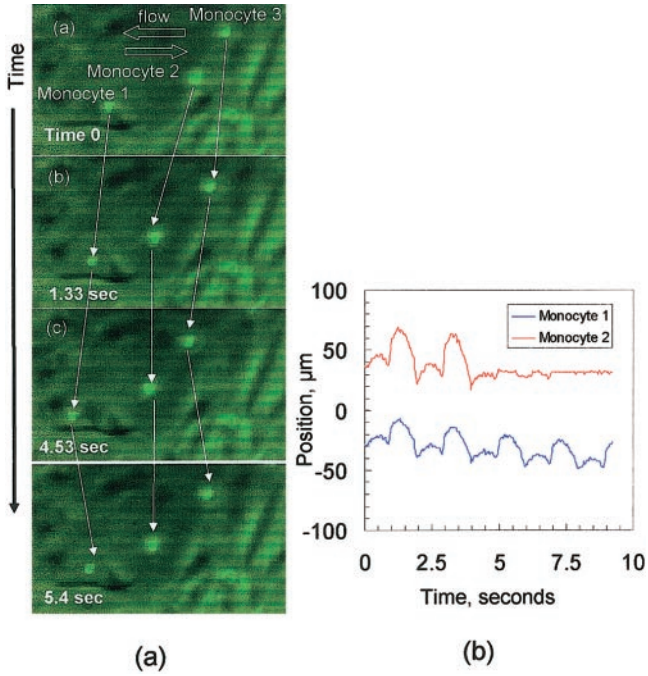

Figure 6. *a)* Captured images of monocyte attachment under oscillatory flow. Note that monocyte 2 established a firm attachment to EC at 4.53 s while monocyte 1 continued to undergo to-and-fro locomotion. *b)* Displacement tracings of monocytes 1 and 2 corresponding to the captured images using cell tracking velocimetry.

P-selectin and ICAM-1 mRNA expression in the oscillatory flow milieu

Expression of adhesion molecules and the counter receptors mediate the cell–cell interactions for the initial capturing of monocytes from the flow field. We demonstrated that P-selectin mRNA expression was up-regulated by 3.4-fold (5.1±0.3; 1.5±0.1, $P<0.05$, n=5) while ICAM-1 was up-regulated by 10.5-fold in response to oscillatory vs. pulsatile shear stress

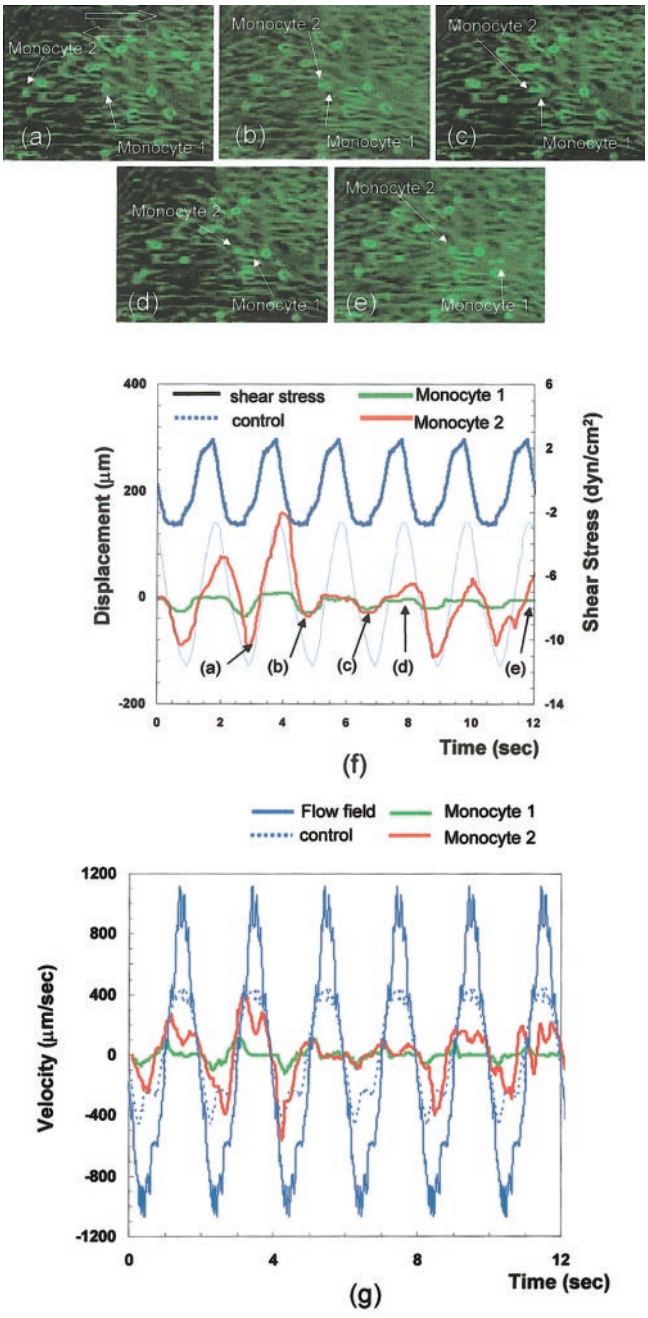

Figure 7. Captured images of cell–cell interactions under oscillatory shear stress. *a)* Monocyte 1 was undergoing tethering while monocyte 2 was in to-and-for locomotion; *b)* monocytes 1 and 2 established binding; *c)* monocytes 1 and 2 started to separate; *d)* monocytes 1 and 2 were apart; *e)* monocyte 2 resumed to-and-fro locomotion while monocyte 1 remained attached to EC. *f)* The dark blue profile reflects the real-time oscillatory shear stress. The trajectories of monocytes 1 and 2 from the captured images (*a–e*) are superimposed with the dotted blue trajectory of the nonviable monocyte (control). *g)* Velocity profiles of monocytes 1 and 2 are compared with that of the nonviable monocyte (control) in relation to the velocity of oscillating flow field.

(26.5±3.3; 2.5±0.7, $P<0.05$, $n=5$) (**Fig. 9**) However, the nonviable monocyte, which failed to harbor counter receptors, displayed trajectory and velocity profiles similar to the direction and periodicity of those of the flow field. Therefore, the relative levels of biochemical and biomechanical forces in the regulation of cell–cell binding kinetics may be determined by the arterial geometry in which pulsatile vs. oscillatory flows develop.

Effects of pulsatile vs. oscillating shear stress on monocyte/EC binding and MCP-1 mRNA expression

Oscillatory flow, which is representative of expected flow at a typical reattachment point in the arterial bifurcation, induced a significant increase in the distribution and probability of monocytes binding to EC (static control=5±2 monocytes/HPF, oscillatory flow=36 ± 4, $P<0.05$) (**Fig. 10*b***). In contrast, unidirectional pulsatile flow, which is representative of expected flow at a typical long straight portion of artery, significantly attenuated monocyte binding to the EC (4±1 monocytes/HPF, $P<0.05$) (Fig. 10*a*). Oscillatory shear stress up-regulated of MCP-1 mRNA expression by 4.8-fold compared with pulsatile flow conditions (8.47±0.63; 1.75±0.63; $P<0.05$, $n=5$; Fig. 10*d*). Thus, the relative MCP-1 mRNA expression correlated with the extent of monocyte bound (Fig. 10*d*).

DISCUSSION

This report introduces MEMS shear stress sensors and cell tracking velocity as powerful tools that permit dynamic real-time quantification and visualization of cell–cell interactions. In addition to providing temporal and spatial resolution of single monocyte locomotion with a time resolution of 0.004 s, the distinct behaviors of monocyte/EC binding kinetics were revealed in response to oscillatory shear stress at ± 2.6 dyn/cm^2. Nonviable monocytes moved according to the direction of shear stress, whereas motion of monocytes on the EC monolayers was retarded, suggesting the critical roles of adhesion molecules and integrins at the reattachment point. Up-regulation of adhesion molecules and cytokines in response to the oscillatory nature of shear stress ($\tau_{ave}=0$) affected the duration of transient tethering and subsequent attachment. The increase in residence time for the individual monocyte under oscillatory flow is conducive to receptors binding to sufficient ligand over the duration of intercellular contact against shear stress induced detachment. We demonstrated the unique behavior of cell–cell interactions in which a sequence of bond formation breakage events occurred causing the monocytes to undergo to-and-fro rolling, transient tethering before firm reattachment on the undulating EC surface.

Shear environment in the vasculature provides the dynamics and molecular constituents necessary to mediate leukocyte-EC adhesion. Not only the magnitude, but also the temporal component of shear stress, is critical in regulating the adhesive interactions. The binding kinetics, which was mediated by adhesion molecules such as selectin and integrin, was reported to

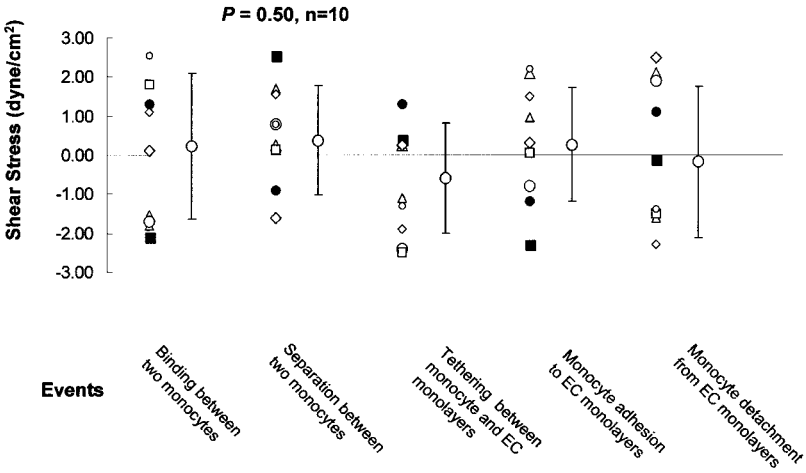

Figure 8. Range of shear stress over which 5 distinct cell–cell interactions occurred: *1)* monocyte-monocyte binding or *2)* separation, *3)* monocyte tethering or *4)* adhesion to EC monolayers, and *5)* monocyte detachment from EC monolayers. The difference among the mean shear stress (open circles with error bars) was statistically insignificant (n=10 for each event, P=0.50) for the individual events.

range from 4 to 7 dyn/cm^2 (27). Shear stress has been implicated in modulating the kinetics and receptor specificity of polymorphonuclear cell (PMN) tumor cell interactions (28). Frequency of tethering formation in shear flow of neutrophiles to P-selectin was demonstrated to be related to shear rate (s^{-1}) rather than to shear stress (dyne/cm^2) by varying viscosity (29). Furthermore, the kinetics of PMN transmigration through endothelial cell junctions was significantly faster under shear flow than that of PMNs placed under static conditions (30).

We demonstrated a dynamic range of oscillating shear stress over which monocyte/EC binding kinetics occurred (Fig. 8). The nature of oscillatory flow, specifically, low mean shear stress and high shear stress gradient, up-regulated the expression of P-selectin, ICAM-1, and MCP-1mRNA in parallel with increasing number of monocytes bound to EC. In vivo studies have demonstrated the presence of redundant mechanisms in leukocyte recruitment. L and P-selectins appear to be

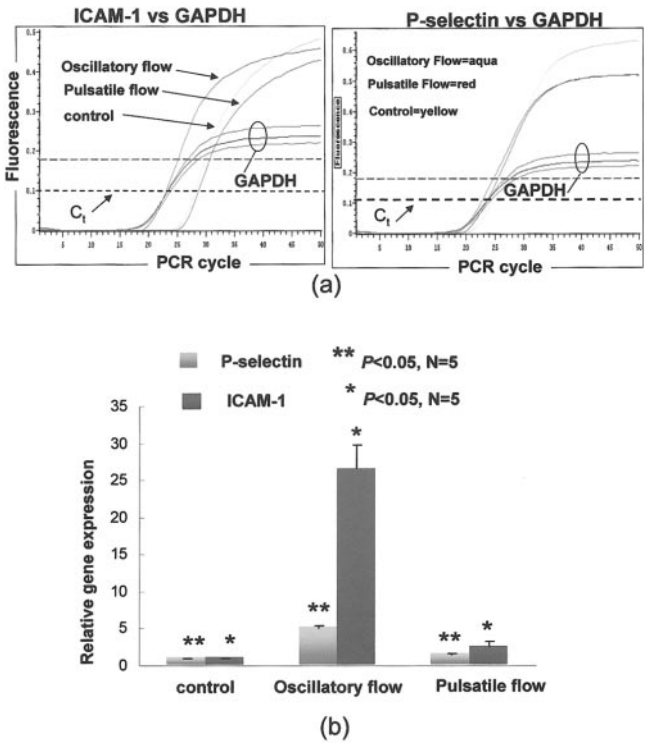

Figure 9. *a)* Fluorescence signal vs. cycle number for P-selectin and ICAM-1 normalized with GAPDH. *b)* Bar graphs show relative mRNA expression for P-selectin and ICAM-1 in response to pulsatile vs. oscillatory flow conditions. Values are expressed as mean ± SE. *P<0.05 P-selectin vs. control; **P<0.05 ICAM-1 vs. control.

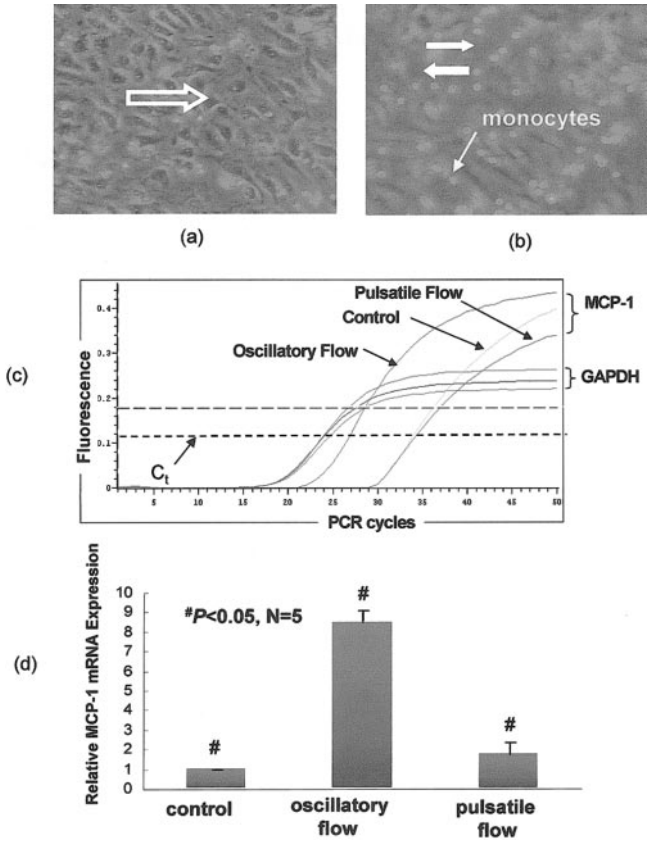

Figure 10. Images of monocyte solid adhesion to EC were captured in response to *a)* pulsatile flow and *b)* oscillatory flow. *c)* Real- time RT-PCR: mRNA expression of MCP-1 and GAPDH in response to control (static condition), oscillatory, pulsatile flow at 4 h; *d)* Relative changes in MCP-1 mRNA expression. Values are expressed as mean ± SE.*P < 0.05 P-selectin vs. control.

primarily responsible for the initial capture of cells from the flowing blood, E and P-selectins for mediating rolling, and β_2 integrins, ICAM-1, and PECAM-1 for adhesion and transmigration (31, 32).The product of arachidonate and complement cascades and chemokines, a large family of small peptides that activate leukocytes via binding to G-protein-coupled receptors, also seem to play fundamental roles in the recruitment process (33, 34). Ramos et al. (1) demonstrated that P-selectin- and VCMA-1-dependent mononuclear cell rolling in $ApoE^{-/-}$ mice was significantly inhibited by mononuclear antibody blockade of P-selectin or its leukocyte ligand P-selectin glycoprotein ligand 1. They also observed that rolling velocities increased after monoclonal antibody blockade of mononuclear cell α_4-integrin or VCAM-1.

The characteristic of oscillatory shear stress has been linked to elevated the oxidative stress in EC by increasing NADH oxidase activity, reactive oxygen species production, and heme oxygenase-1 mRNA expression (35, 36). Therefore, oscillatory flow induces a focal flow milieu in which the expression of cytokines and the activation of receptors/ligands appear be dominant over the dynamic range of shear stress applied in regulating cell–cell interactions.

The present model cannot perfectly replicate the in vivo biochemical milieu at the arterial bifurcation. However, the dynamic visualization displays the nonlinear locomotion of monocytes mediated by the resident time, topology of EC monolayers, integrin-ligand engagement, and expression of cytokines. The constant formation and retraction of filopodial processes may be responsible for the dynamics changes in monocyte morphology, motility patterns, and tethering (37). High-magnification images with high depth of focus (z-axis increments) will be required to allow resolution of fine subcellular structures. The use of vitronectin-coated glass rather than more physiologic substrates may affect cellular responses, since the normal artery wall is compliant and has a more complex extracellular matrix. However, since EC produce their own basement membrane in culture, the substrate in this model is reasonably physiologic. The lack of erythrocytes in the medium may also influence the leukocyte–endothelial interactions. Rolling red cells may collide with, enhance binding of, or displace the leukocytes interacting with EC (38, 39). These effects are likely to be small and of second order. Overall, this modeling provides previously unachievable quantitative analysis. MEMS technology and cell tracking velocimetry demonstrate monocyte /EC focal contact dynamics and variation in binding kinetics in real-time under realistic shear stress fields. These processes are fundamental to the initiation of inflammatory responses.

The microshear stress sensor offers three particularly novel design characteristics: *1)* the heat insulation features a free-standing diaphragm on a vacuum cavity, which minimizes heat loss to the substrate; *2)* the semiconductor material serves as a high-performance heating/sensing element, providing a much higher resistivity than the metal used in conventional thermal sensors; and *3)* the high sensitivity of sensing element allows real-time (frequency >15 kHz) shear stress measurements and a fine spatial resolution comparable to the length of an elongated endothelial cell (<100 μm).

The shear stress sensor is most sensitive when the direction of shear is perpendicular to the width dimension. When the shear stress is at an angle to the longitudinal direction of the sensing element, the sensitivity of the sensor will be proportional to the sine of that angle. The measured sensitivity was 52 uV(ac)/Pa in a gaseous medium and 13.7 uV/V-kPa in a liquid medium (15). The length of the resistive element determines the thermal conduction to the substrate. Longer elements transfer more heat to the substrate but shorter elements confer less sensitivity.

Under oscillatory flow, the shear stress corresponding to flow reversal was recorded in upward deflection from a single sensor. The thermal shear stress operated on heat transfer principle. To better estimate the directionality of shear stress, cross-correlation using a pair of sensors as time dependent events will be indicated.

The optimum resistance range of the micromachined sensor is from 1 to 10 kΩ, much higher than that of the traditional sensor (5 to 50 Ω). Previously, Liu et al. reported the measured time constant to be 72 μs for the MEMS sensors (15). According to the approximate relation between the time constant t_c and cut-off frequency f_c at constant temperature, $f_c = 1/(1.5\ t_c)$, the cut-off frequency is estimated as 9 kHz. This property of the MEMS shear stress sensors contributes to their achieving high-frequency responses.

CONCLUSIONS

Real-time shear stress and cell tracking velocimetry provide a window into the dynamics of monocyte behaviors in response to oscillatory flow. The dynamic visualization of cell–cell interactions revealed the nonlinear and nonrandom binding kinetics of monocytes that were not observable by standard histological cell culture techniques. Within the dynamic range of oscillatory shear stress, the variations in individual monocyte movement are dependent on the expression of adhesion molecules cytokine gradients in a microfluidic environment in which integrin–ligand interactions, with formation and retraction of filopodial processes, governed the dynamic cell–cell contact. The MEMS sensors offer an entry point to directly measure real-time oscillatory shear stress with unprecedented temporal and spatial resolution. The formation of cell–cell binding in the shear environment, visualized as to-and-fro rolling, and transient tethering are largely determined by the relative levels of shear stress, strength of cell–cell adhesion, and cytokine expression. FJ

T.K.H. is supported by AHA BGIA (0265166U) and the National Institutes of Health Career Development Award (K08 HL068689-01A1). This work was also supported by the

Defense Advanced Research Projects Agency (DARPA) Bioflip Project and by the National Institutes of Health NRSA #HL07895. The authors would like to express gratitude to Dr. Wendy Mack for her assistance in statistics.

REFERENCES

1. Traub, O., and Berk, B. C. (1998) Laminar shear stress: mechanisms by which endothelial cells transduce an atheroprotective force. *Arterioscler. Thromb. Vasc. Biol.* **18,** 677–685
2. Malek, A. M., Alper, S. L., and Izumo, S. (1999) Hemodynamic shear stress and its role in atherosclerosis. *J. Am. Med. Assoc.* **282,** 2035–2042
3. Fung, Y. C., and Liu, S. Q. (1993) Elementary mechanics of the endothelium of blood vessels. *J. Biomech. Eng.* **115,** 1–12
4. DePaola, N., Gimbrone, M. A., Jr., Davies, P. F., and Dewey, C. F., Jr. (1992) Vascular endothelium responds to fluid shear stress gradients. *Arterioscler. Thromb.* **12,** 1254–1257 (published erratum appears in *Arterioscler. Thromb.,* 1993 vol. 13, p. 465)
5. Frangos, J. A., Huang, T. Y., and Clark, C. B. (1996) Steady shear and step changes in shear stimulate endothelium via independent mechanisms–superposition of transient and sustained nitric oxide production. *Biochem. Biophys. Res. Commun.* **224,** 660–665
6. Helmlinger, G., Berk, B. C., and Nerem, R. M. (1995) Calcium responses of endothelial cell monolayers subjected to pulsatile and steady laminar flow differ. *Am. J. Physiol.* **269,** C367–C375
7. Ku, D. N., Giddens, D. P., Zarins, C. K., and Glagov, S. (1985) Pulsatile flow and atherosclerosis in the human carotid bifurcation. Positive correlation between plaque location and low oscillating shear stress. *Arteriosclerosis* **5,** 293–302
8. Ravensbergen, J., Ravensbergen, J. W., Krijger, J. K., Hillen, B., and Hoogstraten, H. W. (1998) Localizing role of hemodynamics in atherosclerosis in several human vertebrobasilar junction geometries. *Arterioscler. Thromb. Vasc. Biol.* **18,** 708–716
9. Zarins, C. K., Giddens, D. P., Bharadvaj, B. K., Sottiurai, V. S., and Mabon, R. F. (1983) Carotid bifurcation of plaque localization with flow velocity profiles and wall shear stress. *Circulation Res.* **53,** 502–514
10. Ross, R. (1999) Atherosclerosis is an inflammatory disease. *Am. Heart J.* **138,** S419–S420
11. Glagov, S., Zarins, C., Giddens, D. P., and Ku, D. N. (1988) Hemodynamics and atherosclerosis. Insights and perspectives gained from studies of human arteries. *Arch. Pathol. Lab. Med.* **112,** 1018–1031
12. Ku, D. N. (1997) Blood flow in arteries. *Annu. Rev. Fluid Mech.* **29,** 399–434
13. Pedersen, E., Agerbaek, M., Kristensen, I., and Yoganathan, A. (1997) Wall shear stress and early atherosclerotic lesions in the abdominal aorta in young adults. *Eur. J. Vasc. Endovasc. Surg.* **13,** 4439–451
14. Steinman, D. A., Thomas, J. B., Ladak, H. M., Milner, J. S., Rutt, B. K., and Spence, J. D. (2002) Reconstruction of carotid bifurcation hemodynamics and wall thickness using computational fluid dynamics and MRI. *Magn. Reson. Med.* **47,** 149–159
15. Liu, C., Huang, J. B., Zhu, Z., Jiang, F., Tung, S., Tai, Y.-C., and Ho, C.-M. (1999) A Micromachined flow shear-stress sensor based on thermal transfer principles. *J. MEMS* **8,** 90–99
16. Motomiya, M., and Karino, T. (1984) Flow patterns in the human carotid artery bifurcation. *Stroke* **15,** 50–56
17. Haritonnidis, J. H. (1989) The measurement of shear stress in fluid mechanics measurements. In *Advances in Fluid Mechanics Measurements* (Gad-El-Hak, M., ed) pp. 229–236, Springer-Verlag, New York
18. Huang, J. B., Ho, C. M., Tung, S., Liu, C., and Tai, Y. C. (1995) Micro thermal shear stress sensors with and without cavity underneath. *Proceedings.* IEEE Instrumentation and Measurement Conference, Waltham, MA, Apr. 1995.
19. Hsiai, T. K., Cho, S. K., Honda, H. M., Hama, S., Navab, M., Demer, L. L., and Ho, C. M. (2002) Endothelial cell dynamics under pulsating flow: significance of high- vs. low shear stress slew rates. *Ann. Biomed. Engin.* **30,** 646–656
20. Hsiai, T. K., Cho, S. K., Reddy, S., Hama, S., Navab, M., Demer, L. L., Honda, H. M., and Ho, C. M. (2001) Pulsatile flow regulates monocyte adhesion to oxidized lipid-induced endothelial cells. *Arterioscler. Thromb. Vasc. Biol.* **21,** 1770–1776
21. Raffel, M., Willert, C., and Kompenhans, J. (1998) *Particle Image Velocimetry, A Practical Guide,* Springer-Verlag, Berlin
22. Shanmugan, K., and Breipohl, A. (1988) *Random Signals: Detection, Estimation and Data Analysis,* John Wiley & Sons, New York
23. Fogelman, A. M., Elahi, F., Sykes, K., Van Lenten, B. J., Territo, M. C., and Berliner, J. A. (1988) Modification of the Recalde method for the isolation of human monocytes. *J. Lipid Res.* **29,** 1243–1247
24. Chu, Y., Heistad, D. D., Knudtson, K. L., Lamping, K. G., and Faraci, F. M. (2002) Quantification of mRNA for endothelial NO synthase in mouse blood vessels by real-time polymerase chain reaction. *Arterioscler. Thromb. Vasc. Biol.* **22,** 611–616
25. Walker, N. J. (2002) A technique whose time has come. *Science* **296,** 557–559
26. Livak, K. J., and Schmittgen, T. D. (2001) Analysis of relative gene expression data using real-time quantitative PCR and the 2-Delta Delta CT Method. *Methods* **25,** 402–408
27. Taylor, A. D., Neelamegham, S., Hellums, J. D., Smith, C. W., and Simon, S. I. (1996) Molecular dynamics of the transition from L-selectin- to beta 2-integrin-dependent neutrophil adhesion under defined hydrodynamic shear. *Biophys. J.* **71,** 3488–3500
28. Jadhav, S., Bochner, B. S., and Konstantopoulos, K. (2001) Hydrodynamic shear regulates the kinetics and receptor specificity of polymorphonuclear leukocyte-colon carcinoma cell adhesive interactions. *J. Immunol.* **167,** 5986–5993
29. Chen, S., and Springer, T. A. (2001) Selectin receptor-ligand bonds: Formation limited by shear rate and dissociation governed by the Bell model. *Proc. Natl. Acad. Sci. USA* **98,** 950–955
30. Kitayama, J., Hidemura, A., Saito, H., and Nagawa, H. (2000) Shear stress affects migration behavior of polymorphonuclear cells arrested on endothelium. *Cell. Immunol.* **203,** 39–46
31. Chappell, D. C., Varner, S. E., Nerem, R. M., Medford, R. M., and Alexander, R. W. (1998) Oscillatory shear stress stimulates adhesion molecule expression in cultured human endothelium. *Circ. Res.* **82,** 532–539
32. Rosenfekd, M. E. (2002) Leukocyte recruitment into developing atherosclerotic lesions: The complex interaction between multiple molecules keeps getting more complex. *Arterioscler. Thromb. Vasc. Biol.* **22,** 361–363
33. Aiello, R. J., Bourassa, P. A., Lindsey, S., Weng, W., Freedman, A., and Showell, H. J. (2002) Leukotriene B4 receptor antagonism reduces monocytic foam cells in mice. *Arterioscler. Thromb. Vasc. Biol.* **22,** 443–449
34. Bazan, J. F., Bacon, K. B., Hardiman, G., Wang, W., Soo, K., Rossi, D., Greaves, D. R., and Zlotnik, A. and Schall, T. J. (1997) A new class of membrane-bound chemokine with a CX3C motif. *Nature (London)* **385,** 640–644
35. De Keulenaer, G. W., Chappell, D. C., Ishizaka, N., Nerem, R. M., Alexander, R. W., and Griendling, K. K. (1998) Oscillatory and steady laminar shear stress differentially affect human endothelial redox state: role of a superoxide-producing NADH oxidase. *Circ. Res.* **82,** 1094–1101
36. Ziegler, T., Bouzourene, K., Harrison, V. J., Brunner, H. R., and Hayoz, D. (1998) Influence of oscillatory and unidirectional flow environments on the expression of endothelin and nitric oxide synthase in cultured endothelial cells. *Arterioscler. Thromb. Vasc. Biol.* **18,** 686–692
37. Marschel, P., and Schmid-Schonbein, G. W. (2002) Control of fluid shear response in circulating leukocytes by integrins. *Ann. Biomed. Eng.* **30,** 333–343
38. Schmid-Schonbein, G. W., Usami, S., Skalak, R., and Chien, S. (1980) The interaction of leukocytes and erythrocytes in capillary and postcapillary vessels. *Microvasc. Res.* **19,** 45–70
39. Melder, R. J., Yuan, J., Munn, L. L., and Jain, R. K. (2000) Erythrocytes enhance lymphocyte rolling and arrest in vivo. *Microvasc. Res.* **59,** 316–322

Received for publication November 4, 2002.
Accepted for publication September 1, 2003.